IVYSPRING INTERNATIONAL PUBLISHER

Theranostics

2017; 7(16): 4029-4040. doi: 10.7150/thno.19538

Research Paper

Investigating the Effect of Chemical Structure of Semiconducting Polymer Nanoparticle on Photothermal Therapy and Photoacoustic Imaging

Dongdong Li[1]*, Guobing Zhang[2]*, Weiguo Xu[3]*, Junxia Wang[1], Yucai Wang[4]✉, Longzhen Qiu[2], Jianxun Ding[3]✉, Xianzhu Yang[1]✉

1. Institutes for Life Sciences, School of Medicine and National Engineering Research Center for Tissue Restoration and Reconstruction, South China University of Technology, Guangzhou, Guandong 510006, P.R. China;
2. Academy of Opto-Electronic Technology, Hefei University of Technology, Hefei, Anhui 230009, P.R. China;
3. Key Laboratory of Polymer Ecomaterials, Changchun Institute of Applied Chemistry, Chinese Academy of Sciences, Changchun 130222, P. R. China;
4. School of Life Sciences and Medical Center, University of Science & Technology of China Hefei, Anhui 230027, P.R. China.

* These authors contributed equally to this work.

✉ Corresponding authors: E-mail: yangxz@scut.edu.cn (Xianzhu Yang), E-mail: jxding@ciac.ac.cn (Jianxun Ding), and E-mail: yucaiwang@ustc.edu.cn (Yucai Wang)

Received: 2017.02.07; Accepted: 2017.05.29; Published: 2017.09.20

Abstract

The donor-acceptor semiconducting polymers (SPs) have robust absorbance in near-infrared (NIR) region, great photostability, high photothermal conversion efficiency, and good biocompatibility. Thus, the SPs exhibit great potentials for photothermal therapy (PTT) and photoacoustic imaging (PAI). However, poor understanding of the underlying mechanisms and the correlation between the SP polymer chemical structures and their performances of PTT and PAI have significantly hindered their biomedical application. Herein, a series of acceptor–π–acceptor type (A1–π–A2) type SPs were synthesized. The diketopyrrolopyrrole (DPP) and thiophene are used as A1 electron accepting block and π-bridge, and the chemical structure of A2 unit was variable. The SPs were formulated into PEGylated nanoparticles, which ensured these SP-based nanoparticles (SP@NPs) exhibited similar size, shape, and physiological stability. Thus, the chemical structure of A2 unit was the only variable. The effects of the SP chemical structures are carefully and comprehensively evaluated through both *in vitro* and *in vivo* experiments. Our results demonstrated the chemical structure of A2 unit simultaneously impact their absorption spectra and photothermal (PT) conversion efficiency, which finally determined their PTT and PAI performances. Among these A2 acceptors, thieno[3,2-b]thiophene (TT) unit exhibited the best *in vitro* and *in vivo* anticancer efficacies and PAI performances. This study not only provides molecular insights into the design of efficient SPs for PTT and PAI but also highlights the flexibility and potential of SP@NPs for biomedical application. Thus, SP@NPs can act as a versatile nanoplatform for the development of novel light intensive imaging and therapeutic approaches.

Key words: semiconducting polymer, donor-acceptor polymer, photothermal therapy, photostability, photoacoustic imaging.

Introduction

The nanomaterials with strong absorbance in the near-infrared (NIR) region exhibit an immense potential as photothermal (PT) and photoacoustic (PA) contrast agents for cancer therapy and diagnosis [1-6]. The absorbed light energy can efficiently transform into PT effect and are accompanied by other phenomena such as PA waves, microbubbles and so on. Until now, many nanomaterials, which included noble metals nanostructures [7-9], carbon nanomaterials [10-12], copper sulfide nanoparticles [13-15], porphysomes [16-18], organic NIR dyes [19-21], have been explored as PT and PA contrast

agents. However, organic dyes and metallic nanoparticles usually have poor photostability; carbon nanotubes and graphenes encounter the issue of broad NIR absorbance peaks, and porphysomes have phototoxicity [22-25]. Thus, it is still highly desirable to exploit new optical PT and PA contrast agents.

The donor-acceptor semiconducting polymers (SPs), which have been widely used for organic photovoltaics and field-effect transistors, have sharp and robust NIR absorbance peaks [26-29]. As reported, the SPs demonstrated great photostability, high PT conversion efficiency, and possessed good biocompatibility [30, 31]. Several groups have reported the use of semiconducting polymers for PT cancer therapy, such as polyaniline [32, 33], poly(3,4-ethylenedioxythiophene):poly(4-styrenesulfonate) [34, 35], polypyrrole [36-38], and so forth. Additionally, semiconducting polymers have been used as PA molecular imaging probes in living mice by Rao and coworkers [22, 30, 39, 40]. The SPs as the PT and PA contrast agents have shown great promise for cancer therapy and diagnosis. However, until now, it is unclear how the SP polymer chemical structure affects its PTT and PAI performance. Recently, pioneering work has firstly confirmed chemical structures of SPs play an important role in determining PA signal brightness and PTT effect [22, 23]. Thus, understanding the relationship between the SP polymer chemical structure and its performance of PTT and PAI was essential to establish principles for the rational design in the future. Unfortunately, relevant research was still rarely reported.

Herein, we designed a new series of acceptor–π–acceptor (A1–π–A2) type SPs to investigate the correlation between the SP polymer chemical structure and its PTT/PAI performance. The DPP and thiophene are used as A1 electron accepting block and π-bridge, and the chemical structure of A2 could be regulated by changing the monomer structure during Stille cross-coupling polymerization (Scheme S1). We formulated the obtained A1–π–A2 SPs into PEGylated nanoparticles through single emulsion methods under the assistance of an amphiphilic diblock copolymer poly(ethylene glycol)-*block*-poly(hexyl ethylene phosphate) (mPEG-*b*-PHEP) (Figure 1A). Thus, these SP-based nanoparticles exhibited similar nanoproperties, including size, shape, zeta potentials, and physiological stability, leaving chemical structure of A2 unit as the only variable to be studied. We systematically and comprehensively evaluated chemical structure of A2 unit on absorption, PT conversion, photostability, PAI, and overall antitumor efficacy. Our results clearly demonstrated that regulating chemical structure of SPs is a new avenue to fabricate the next generation of PT and PA contrast agents with superior performance.

Materials and Methods

Materials and general characterizations

3-(4,5-Dimethylthiazol-2-yl)-2,5-diphenyl tetrazolium bromide (MTT) was obtained from Sigma-Aldrich (Shanghai, P. R. China). Dulbecco's Modified Eagle Medium (DMEM), fetal bovine serum (FBS) and L-glutamine were purchased from Gibco BRL (Eggenstein, Germany). Ultra-purified water was obtained using a Milli-Q Synthesis System (Millipore, Bedford, MA, USA). The diblock polymer mPEG-*b*-PHEP was synthesized using mPEG-OH (number-average molecular weight (*Mn*) = 2,000 g/mol) as the macroinitiator as described previously [24]. These SPs were synthesized as described in the Supporting Information. Other organic solvents or reagents were used as received.

The size and size distribution of the polymeric nanoparticles were measured by DLS, which was carried out on a Malvern Zetasizer Nano ZS90 with a He–Ne laser (633 nm) and 90° collecting optics. The data were analyzed by Malvern Dispersion Technology Software 4.20. The absorption spectra were measured on a UV-3802 (UNICO, P. R. China) spectrophotometer. The transmission electron microscope (TEM, JEOL-2010, Japan) measurements were carried out with an acceleration voltage of 200 kV.

Preparation of nanoparticles SP@NPs

A chloroform ($CHCl_3$) (200 μL) containing mPEG-*b*-PHEP (10.0 mg) and SPs (1.0 mg) and ultrapurified water (1.0 mL) were emulsified by sonication for 2 minutes (work 5 seconds and rest 2 seconds) at 325 W output using a microtip probe sonicator (JY92-IIN, Scientz biotechnology, Ningbo, China). The solution was further stirred under reduced pressure for 30 min to evaporate the organic solvent, and then purified by passing through a 0.45 μm filter (Millipore). No precipitation was found by this method. A standard curve was obtained by plotting the absorbance of the SPs against its concentration (in $CHCl_3$). The obtained nanoparticles SP@NPs were lyophilized and re-dissolved in $CHCl_3$, and then the encapsulating efficacy was calculated according to this standard curve, reaching *ca.* 98%.

In vitro PT effects

The aqueous solution of SP@NPs in centrifuge tube was irradiated by an 808 nm diode laser (BWT Beijing Ltd., P. R. China) at a power density of 2.0 W/cm^2. Ultrapure water irradiated at the same

conditions was used as a control. The changes in temperature were monitored by an infrared camera (ICI7320, Infrared Camera Inc., USA) and analyzed using IR Flash thermal imaging analysis software (Infrared Cameras Inc., USA).

In vitro PA performance

For *in vitro* PAI, the SP@NPs dispersions at various concentrations (2.0, 4.0, 6.0, 8.0, and 10.0 μg/mL) were loaded into agar gel cylinders (diameter ~1.0 cm), and then imaged on multispectral optacoustic tomographic (MSOT) imaging system equipped with 128 ultrasound transducer elements (inVision 128, iThera Medical, Germany). The PA signals were collected under 808 nm wavelength excitation light. The PA signal of each sample was calculated by averaging over the region of sample.

Photostability of SP@NPs for PTT and PAI

The SP@NPs at a concentration of 30.0 μg/mL were exposed to NIR laser (808 nm, 2.0 W/cm^2, 15 min, laser on). Subsequently, the NIR laser was turned off for 15 min, and the solution was naturally cooled to room temperature (laser off). The laser on and laser off cycles were repeated for four times. The change in temperature and the thermal imaging were monitored as described above. Meanwhile, the absorbance spectrum of the irradiated samples was examined after the last NIR irradiation.

In vitro PT cytotoxicity of SP@NPs

Breast cancer cells MDA-MB-231 (American Type Culture Collection, Rockefeller, Maryland, USA), were seeded in a 96-well plate (1×10^4 cells per well) at 37 °C with 5% CO_2 overnight. The medium was replaced by fresh media containing SP@NPs at different concentrations of SPs. After incubation for 4 h, the cells were exposed to NIR laser (808 nm, 1.0 W/cm^2, 10 min). Further incubated for 24 h, and then the cell viability was analyzed by MTT assay. Meantime, after treated with these SP@NPs at a concentration of 40.0 μg/mL for 4 h and then irradiated by NIR (808 nm, 1.0 W/cm^2, 10 min), the tumor cells were rinsed by PBS twice and stained by live/dead viability/cytotoxicity kit (Invitrogen, USA). Live and dead cells were then imaged with fluorescence microscope (Nikon TE 2000-U, Japan).

In addition, the PT cytotoxicity of SP@NPs nanoparticles at different power densities was also examined. The tumor cells were seeded in 96-well plates as described above. After incubation overnight, the fresh media containing SP@NPs nanoparticles (30.0 μg/mL SP) were added. After 4 h of incubation, the cells were exposed to different power densities laser for 10 min, further cultured for 24 h, and then the cell viability was analyzed.

In vivo PAI of SP@NPs in matrigel and their photostability

In order to compare the *in vivo* PAI signal of these SP@NPs, the nanoparticle solutions were suspended in Matrigel (BD Biosciences) at a SP concentration of 50.0 μg/mL, and the final concentration of Matrigel was 50% v/v for all solutions. Matrigel-nanoparticle mixtures (30.0 μL) were injected subcutaneously on the dorsal aspects of female nude mice to form inclusions of nanoparticles, and PAI was performed using the MSOT imaging system at 808 nm.

Animal and tumor model

Female BALB/c nude mice (20±2 g, 6-8 weeks old) were purchased from Beijing HFK Bioscience Co. Ltd. The procedures were approved by the Hefei University of Technology Animal Care and Use Committee, and all animals received care in compliance with the guidelines outlined in the Guide for the Care and Use of Laboratory Animals. MDA-MB-231 cells (2 × 10^6) cells were injected into the mammary fat pads of female BALB/c nude mice to establish a human breast cancer xenograft tumor model. The mice were used for *in vivo* experiments when the tumor volumes reached 60 mm^3.

In vivo PAI of tumor by SP@NPs

Mice bearing MDA-MB-231 tumors were intravenously administrated with 200 μL of the SP@NPs nanoparticles at a SP dose of 40 μg per mice. At the predetermined times, the mice were anaesthetized with 2% isoflurane and placed into the MSOT system. Then, the PAI signals of tumor were acquired at 808 nm.

In vivo PTT efficacy of SP@NPs

Mice bearing MDA-MB-231 tumors were intratumorally administrated with 40 μL of SP@NPs nanoparticles at a SP dose of 40 μg per mice, and mice treated with the same volume of saline were used as the control. Then, after 2 h postinjection, the tumor tissues of these mice were irradiated with NIR laser (808 nm, 0.5 W/cm^2, 10 min). The temperature of the tumor sites were detected by IR 7320 thermal camera. Additionally, the tumor volumes were measured by a caliper and calculated based on the following equation: tumor volume (mm^3) = length × width^2 × 0.5. After treatment for two weeks, the tumor tissues of killed mice were excised to measure the weight.

Statistical Analysis

To measure significant differences among the treatment groups, statistical analyses were performed

using Student's *t*-test. *$p < 0.05$ were considered to be statistically significant, **$p < 0.01$ and ***$p < 0.001$ were considered to be highly significant.

Results and Discussion

The preparation and characterization of SP-based nanoparticles

To fine turn the chemical structure of SPs, two acceptor units (A1 and A2) were introduced into the semiconducting polymer backbone to replace the customary donor-acceptor structure, and the chemical structure of A2 could be regulated by changing the monomer structure during Stille cross-coupling polymerization as shown in Scheme S1. In these A1–π–A2 type SPs, the DPP unit was selected as the A1 electron acceptor, because DPP-based SPs exhibited show excellent light and thermal stability [22, 23], which makes them suitable for PTT and PAI. Meantime, thiophene was used as π-bridge to conjugate the A1 and A2 electron acceptor. The obtained SPs have different A2 electron acceptor backbone structures (Figure 1B), which are expected to possess a profound impact on their performances of bandgap, absorbance, PT conversion, PTT, and PAI.

These A1–π–A2 type SPs possessed extremely hydrophobic backbone structure, which was unable to evaluate the correlation between chemical structures and the PAI/PTT performance in physiological environments. To endow these polymers with good stability for in vitro and in vivo applications, an amphiphilic polymer mPEG-*b*-PHEP is used to stabilize the A1–π–A2 SPs by single emulsion methods as well as to provide a relatively inert particle surface (Figure 1A). The obtained nanoparticles prepared by the SPs with A2 electron acceptors of PhT, TVT, DPT, and TT are denoted as NP_{PhT}, NP_{TVT}, NP_{DPT}, and NP_{TT}, respectively. All the obtained SPs nanoparticles (SP@NPs) showed similar size at ca. 50 nm according the results of dynamic light scattering (DLS, Figure 1C). Meantime, these SP@NPs are transparent in PBS and PBS containing 10% FBS (Figure 1D), and no obvious size change

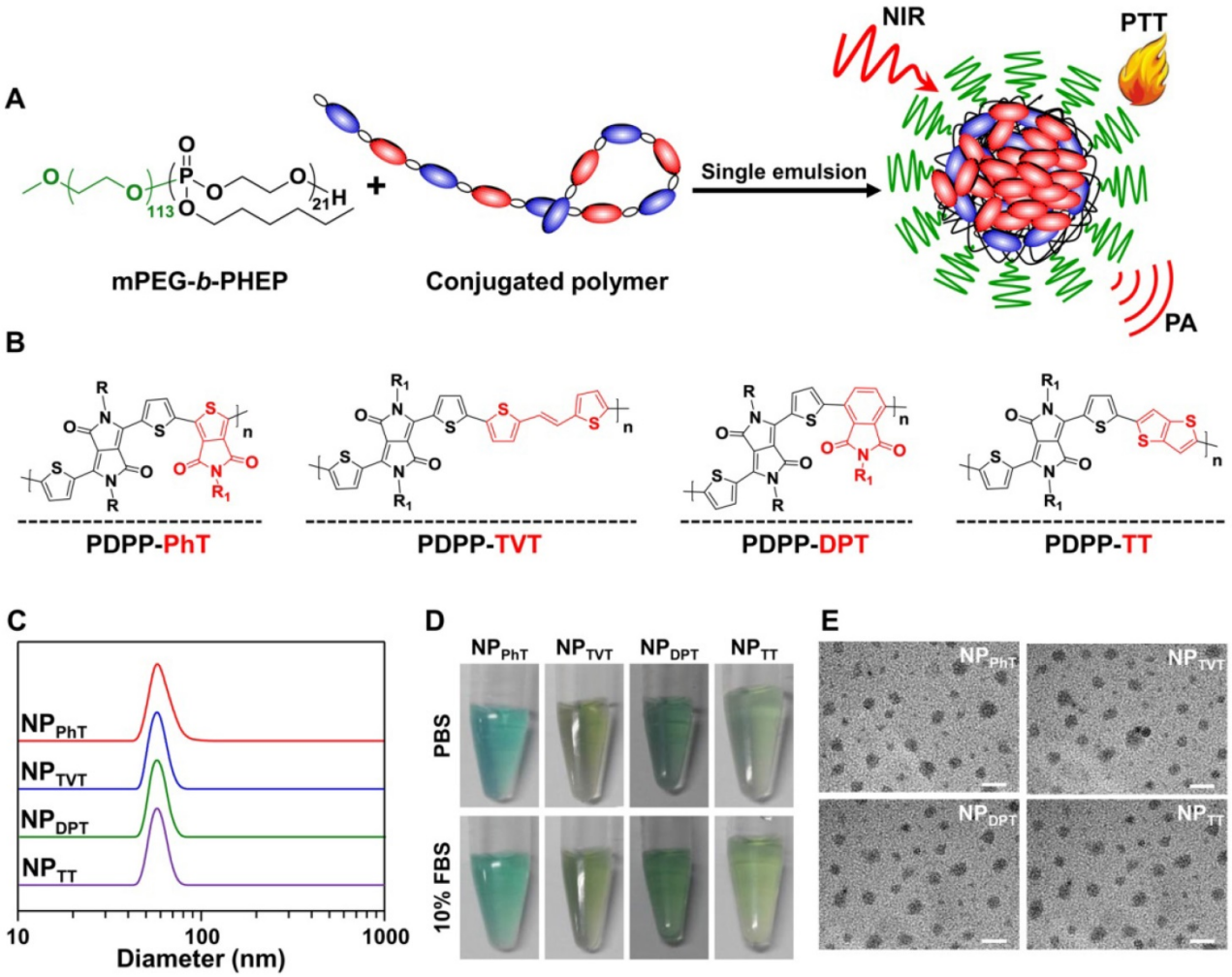

Figure 1. Preparation and characterization of the nanoparticles prepared by SPs with variable A2 units. (A) Scheme illustration of the nanoparticles prepared by these DPP-based SPs with different A2 units (SP@NPs) through single emulsion with the assist of mPEG-*b*-PHEP. (B) Chemical structures of these DPP-based SPs with variable A2 units (PhT, TVT, DPT, and TT). (C, D, E) Size distributions (C), photograph (D), and TEM images (E) of SP@NPs. The scale bars were 100 nm.

within 7 days was observed (Figure S1), which might be due to the stabilization by PEG layer. Additionally, the transmission electron microscope (TEM) images of all SP@NPs (Figure 1E) show a classic spherical structure. These SP@NPs also exhibited similar zeta potentials (ca. -20 mV, Figure S2). These results demonstrated that these SP-based nanoparticles exhibited similar physicochemical properties, including size, shape, and physiological stability, thus the chemical structures of A2 electron acceptor was the only variable to be studied for PTT and PAI performance.

The PTT and PAI performance of SP@NPs with variable A2 electron acceptor

The PT effects of SP@NPs with different A2 electron acceptor were first investigated. The SP@NPs at a SP concentration of 30.0 μg/mL were irradiated by a 808 nm NIR laser for 15 min, and the infrared thermal images of aqueous solution were recorded. As the irradiation time increased, the temperature of the SP@NP solution increased in an order of NP_{TT} > NP_{DPT} > NP_{TVT} > NP_{PhT} (Figure 2A). After irradiation for 15 min, the temperatures of NP_{TT}, NP_{DPT}, NP_{TVT}, and NP_{PhT} increased by 29.3, 18.0, 13.5, and 8.4 °C, respectively. Additionally, the temperatures of all these SP@NPs increased monotonically with increases in concentrations, and the temperature increase of SP@NPs followed this order at each SP concentrations (Figure S3). Moreover, the color of the PT images also easily demonstrated the temperature difference among these SP@NPs (Figure 2B), which indicated the PT effects of SP@NPs are closely associated with their chemical structure of the A2 electron acceptor.

The effects of SP chemical structures on their PAI property were further determined. The aqueous solutions of the SP@NPs at a SP concentration of 10.0 μg/mL were added into agar gel cylinders, and then the PA signals under NIR laser irradiation were acquired on a multispectral optoacoustic tomography (MSOT, inVision 128, iThera Medical, Germany) equipment. As shown in Figure 2C, the PA intensities of SP@NPs follow the same order of their PT effect: NP_{TT} > NP_{DPT} > NP_{TVT} > NP_{PhT}. Moreover, the PA amplitudes of SP@NPs at 808 nm were determined at a series of concentrations from 2.0 to 10.0 μg/mL (Figure 2D). At each concentration, NP_{TT} exhibited the highest PA brightness followed by NP_{DPT}, NP_{TVT}, and NP_{PhT}, and the PA signals intensities of SP@NPs were linearly strengthened with the concentrations of SPs.

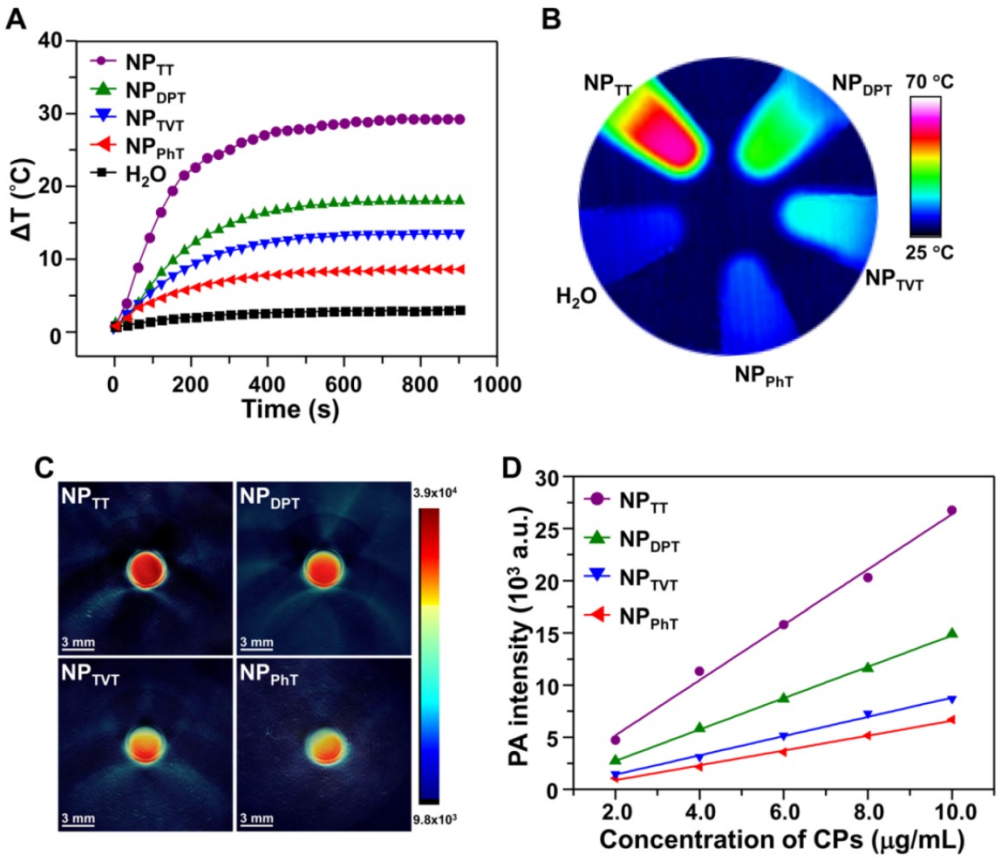

Figure 2. PT and PA properties of the SP@NPs. (A, B) Temperature change curves (A) and thermal image (B) of SP@NPs upon exposure to NIR laser (808 nm, 2.0 W/cm², 15 min). (C) Representative PA images of agar gel cylinder at a SP concentration of 2.0 μg/mL excited by pulsed laser at 808 nm. (D) Linear fitting plots of PA amplitudes *versus* SP concentration in aqueous solutions of SP@NPs under NIR laser irradiation.

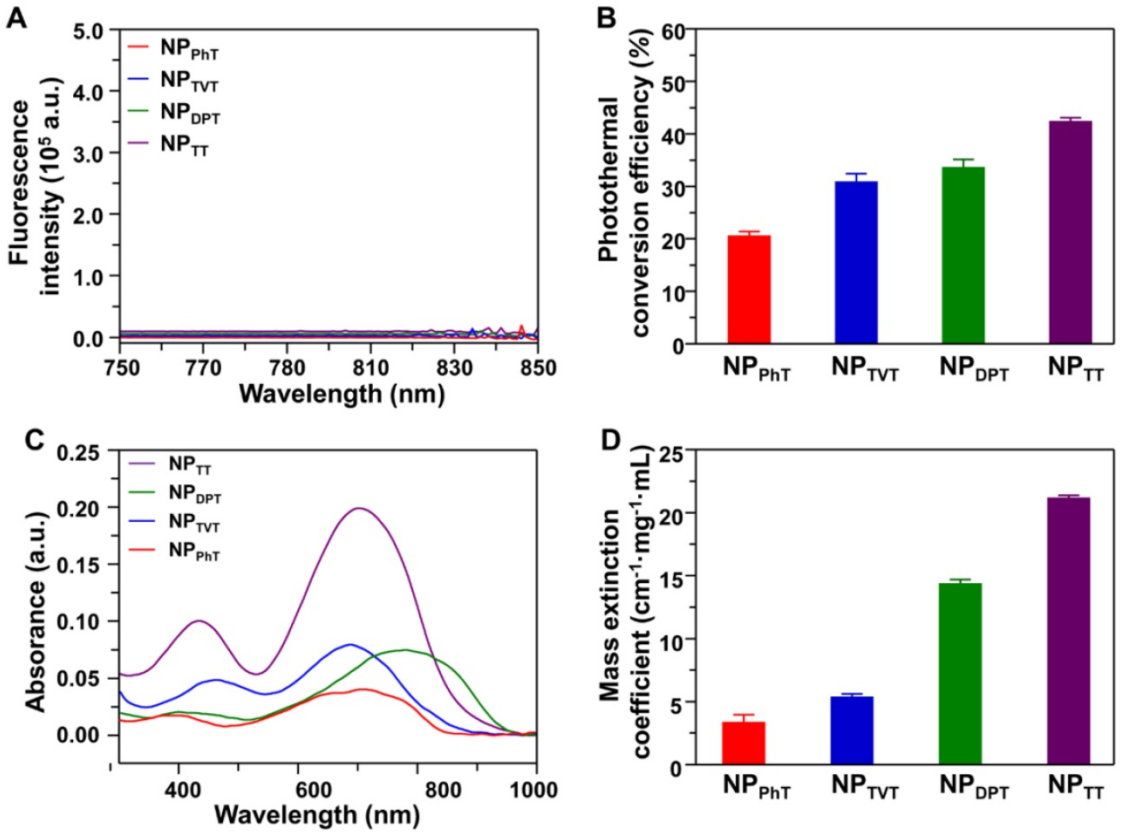

Figure 3. The absorption and dissipation of light energy at 808 nm by these SP@NPs. (A) Fluorescence spectra of NP_{TT}, NP_{DPT}, NP_{TVT}, and NP_{PhT} ([SP] = 10 μg/mL) upon excitation at 808 nm. (B) Photothermal conversion efficiency of NP_{TT}, NP_{DPT}, NP_{TVT}, and NP_{PhT}. (C) Absorption spectra of these SP@NPs with different A2 units ([SP] = 5.0 μg/mL). (D) Mass extinction coefficient of these SP@NPs at 808 nm.

Mechanism of PTT and PAI performances in the order of NP_{TT} > NP_{DPT} > NP_{TVT} > NP_{PhT}

The above results indicated that the PT effect and PA brightness of SP@NPs followed the same order: NP_{TT} > NP_{DPT} > NP_{TVT} > NP_{PhT}. It is well known that the absorbed light energy is generally dissipated through i) fluorescence emission, ii) generation of heat (thermal deactivation), and iii) intersystem conversion to long-lived species (*e.g.*, phosphorescence) [41]. It could be observed that the SP@NPs are not phosphorescent (Figure S4). To demonstrate reason behind the PT effect and PA brightness in such order (NP_{TT} > NP_{DPT} > NP_{TVT} > NP_{PhT}), the fluorescence spectra, PT conversion efficiency, absorption spectra, and mass extinction coefficients of these SP@NPs were determined. The fluorescence spectra of SP@NPs upon excitation at 808 nm are shown in Figure 3A, which indicated that the fluorescence emission of all these SP@NPs was negligible. Therefore, the generation of heat could be the main pathway to dissipate the absorbed energy after NIR irradiation.

Furthermore, the PT conversion efficiencies (η value) of SP@NPs were calculated according to the method developed by Roper *et al.* [42]. As shown in Figure 3B and S5, the η values of NP_{TT}, NP_{DPT}, NP_{TVT}, and NP_{PhT} were calculated to be 42.53%, 33.66%, 30.96%, and 20.66%, respectively. It could be found that NP_{TT} and NP_{PhT} exhibited the highest and the lowest PT conversion efficiencies, respectively. It is interesting that the PT conversion efficiency of NP_{DPT} and NP_{TVT} was almost the same. However, the PT effect and PA brightness of NP_{DPT} were remarkable higher than that of NP_{TVT}. To reveal the reason, the absorption spectra of NP_{PhT}, NP_{TVT}, NP_{DPT}, and NP_{TT} are further detected. As shown in Figure 3C, the NP_{PhT}, NP_{TVT}, NP_{DPT}, and NP_{TT} exhibited the absorption maxima at 714, 690, 781, and 704 nm, respectively. Their maximal absorption peaks were affected by the corresponding bandgaps of these SPs [22, 23], which were 1.44 eV, 1.50 eV, 1.30 eV, and 1.42 eV (Figure S6), respectively. Furthermore, the mass extinction coefficients of SP@NPs were calculated according to their absorption spectra. As shown in Figure 3D, the mass extinction coefficients of NP_{TT}, NP_{DPT}, NP_{TVT}, and NP_{PhT} at 808 nm were 21.2, 14.4, 5.4, 3.4 cm^{-1} mg^{-1} mL, respectively. It could be found that more light energy was absorbed by the NP_{DPT} at the same SP concentration when compared with that of NP_{TVT}. Therefore, the PT effect and PA brightness performance of NP_{DPT} were significantly higher than

that of NP_{TVT} even both NPs exhibited the similar PT conversion efficiency. These results also indicated that the photothermal effect and PA brightness were simultaneously associated with the mass extinction coefficients and photothermal conversion efficiency. The strongest absorbance and the highest PT conversion efficiency at 808 nm ensured the highest PT effect and PAI performance of NP_{TT}, followed by NP_{DPT}, NP_{TVT}, and NP_{PhT}, respectively. Thus, the PT effect and PA brightness follow the order: NP_{TT} > NP_{DPT} > NP_{TVT} > NP_{PhT}.

Photostability of SP@NPs for PT effect and PA brightness

As reported, SPs demonstrated great photostability for PTT therapy and PAI [22, 31]. To verify it, we further investigated the photostability of these SP@NPs. Four cycles of laser on/off (laser on time: 15 min; laser off time: 15 min) with NIR irradiation (808 nm, 2.0 W/cm^2) were performed. Compared to the temperature change after the first laser irradiation, no significant decrease of the temperature elevation for all these SP@NPs was observed for another three additional cycles (Figure 4A). After four laser on/off cycles, the absorption spectra of these SP@NPs were recorded. It was found that the spectrum did not change upon irradiation (Figure S7). Additionally, SP@NPs was exposed to the NIR laser (808 nm, 2.0 W/cm^2) for 15 min, until steady state temperature was reached. Then, the thermal images of SP@NPs under NIR irradiation were recorded by IR camera (Figure 4B). It could be found that the steady state temperature showed a negligible decrease for all SP@NPs, which indicated their excellent NIR photostability. In addition, to further evaluate the photostability of SP@NPs, the change of the PA signal was also detected after exposure to laser pulses for 48 min (Figure 4C). The PA signal of all these SP@NPs showed no obvious intensity loss. This result is similar to that of PT effect, suggesting that all these SP@NPs possess excellent photostability. The excellent phtostability of these SP@NPs might be due to the thermal properties of the semiconducting polymer. We have found that the decomposition temperature at 5% weight loss for PDPP-PhT is above 400 °C, which is high enough for the PT effect and PAI [43].

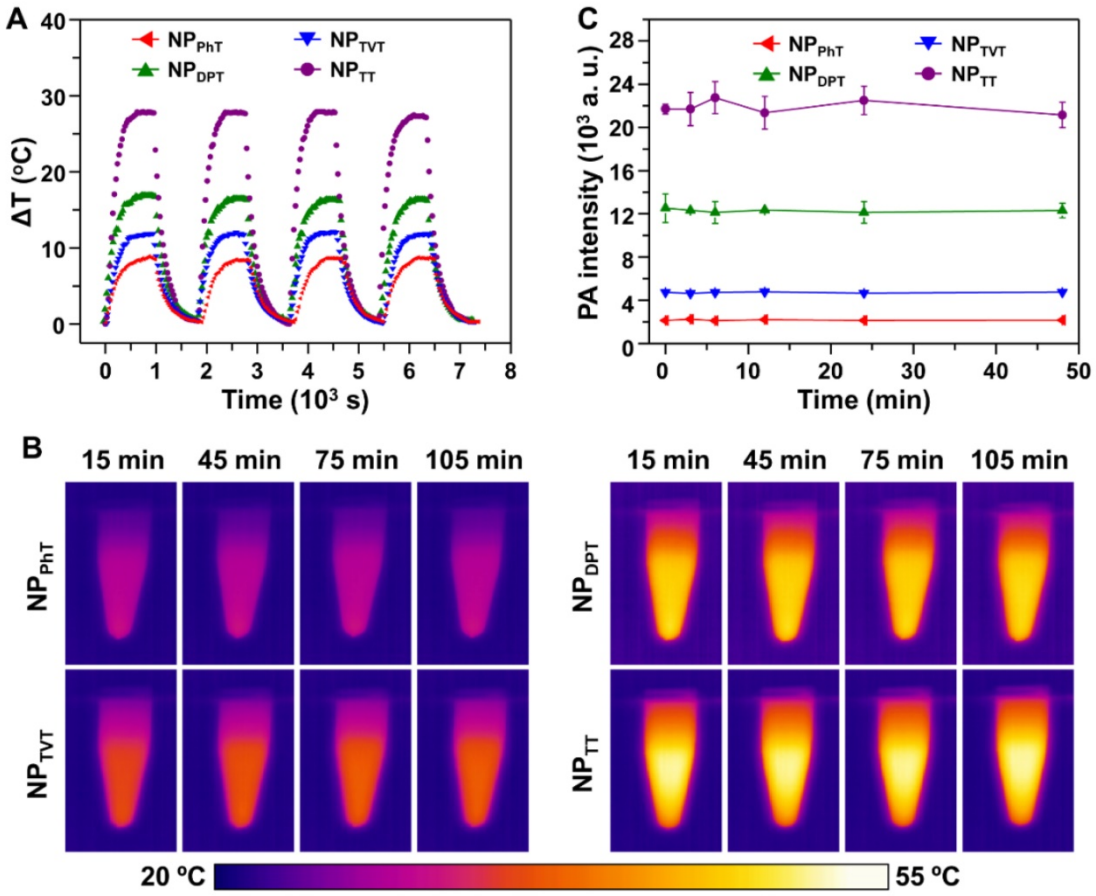

Figure 4. Stability of the PT effect and PA properties of these SP@NPs. (A) Temperature elevation of SP@NPs (30.0 μg/mL) over four laser on/off cycles of NIR irradiation (808 nm, 2.0 W/cm^2, 15 min). (B) Thermal images of SP@NPs as a function of time upon exposure to the NIR laser (808 nm, 2.0 W/cm^2). (C) PA amplitudes of SP@NPs solution excited by pulsed laser at 808 nm as a function of irradiation time.

In vitro PTT therapy of SP@NPs

We further evaluate the effect of chemical structures of the SPs on PTT efficacies by MTT assay. Human breast cancer cells MDA-MB-231 were pre-incubated with these SP@NPs at different concentrations for 4 h, and then irradiated with 808 nm laser at a power density of 1.0 W/cm^2 for 10 min. As shown in Figure 5A, as the concentration of SP was increased, more cells were killed by the NIR irradiation. Among these SP@NPs, NP_{TT} exhibited the strongest anticancer efficacy at each concentration, within a half maximal inhibitory concentrations (IC_{50}) of 13.7 μg/mL, whereas the IC_{50} of NP_{DPT}, NP_{TVT}, and NP_{PhT} were 25.8, 37.8, and 40.1 μg/mL, respectively. The anticancer efficacy of SP@NPs followed the same order of their PT effect: NP_{TT} > NP_{DPT} > NP_{TVT} > NP_{PhT}. It should be noted that the incubation with only these SP@NPs did not exhibit obvious toxicity to MDA-MB-231 cells without NIR light illumination even at the highest concentration (Figure S8).

In addition, after treatment with these SP@NPs as described above, MDA-MB-231 cells were stained by live/dead viability/cytotoxicity kit to evaluate the PT-induced therapeutic efficacy. As shown in Figure 5B, the percentage tumor cells with red fluorescein (dead cells) was gradually increased when the cells were incubated with NP_{TT}, NP_{DPT}, NP_{TVT}, and NP_{PhT}, which were consistent well with the above results. These results indicated that the PT-induced therapeutic efficacies of SP@NPs against cancer cells were both dose-dependent and laser density-dependent, and followed the order of their PT effects: NP_{TT} > NP_{DPT} > NP_{TVT} > NP_{PhT}.

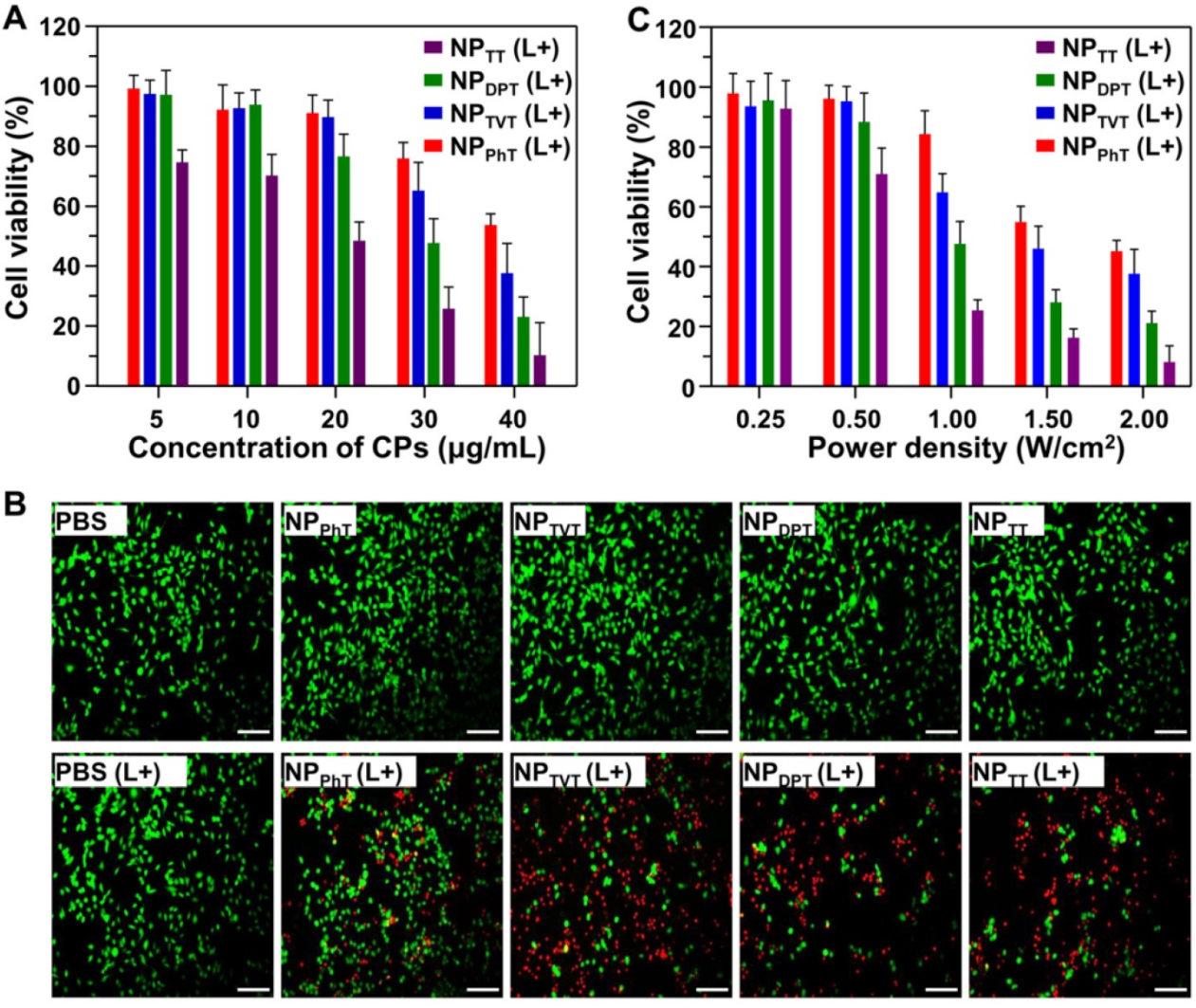

Figure 5. The PT-induced therapeutic efficacy of SP@NPs against cancer cells. (A, B) Relative viabilities of MDA-MB-231 cells after treatment with SP@NPs at different concentrations of SPs (A) or at different power densities (C). All data are presented as mean ± SD (n = 3). (B) Fluorescence images of live/dead staining of MDA-MB-231 cells after treatment with SP@NPs at SP concentrations of 40.0 μg/mL. (L+) represented the cells pre-incubated with different formulations was exposed to NIR irradiation (808 nm, 10 min). The scale bar was 50 μm.

Next, the PT-induced therapeutic efficacies of SP@NPs under different laser powers were also detected by MTT assay. After pre-incubation with SP@NPs at a concentrations of 30.0 μg/mL for 4 h, the cells were exposed to NIR laser (10 min) at 0.25 W/cm², 0.5 W/cm², 1.0 W/cm², 1.5 W/cm², and 2.0 W/cm², respectively. It should be noted that the MDA-MB-231 cells plus NIR light illumination did not affect the cell viability, even at the highest power density (Figure S9). As shown in Figure 5C, for all the SP@NPs, the cell viabilities were decreased as the increase of power density. To induce 50% tumor cell death, the power densities of the NIR were 0.63, 1.03, 1.54 and 1.88 W/cm² for NP_{TT}, NP_{DPT}, NP_{TVT}, and NP_{PhT}, respectively.

PT effect and PAI properties of these SP@NPs *in vivo*

Followed by examining the effect of chemical structures of the SPs on PTT efficacy *in vitro*, we further investigated the PT effect and PAI in a tumor model. To avoid interference by tumor accumulation of these SP@NPs, mice bearing MDA-MB-231 tumor were firstly intratumorally injected with NP_{TT}, NP_{DPT}, NP_{TVT}, and NP_{PhT} at a SP dose of 40 μg per mouse. Subsequently, the tumor site was irradiated by 808 nm NIR laser for 10 min, and the local temperature change was recorded by the infrared thermal camera. The mice injected with PBS was also been investigated as the control groups. As shown in Figure 6A, as the irradiation time increased, the color of the PT images in tumor site continuously changed from purple (low temperature) to bright yellow (high temperature). Among SP@NPs, the NP_{TT} group exhibited the highest temperature increase, followed by $NP_{DPT,}$ while NP_{TVT} and NP_{PhT} only showed slight temperature increase. The quantitative tumor temperature curve was showed in Figure 6B. It could be found that the temperature of the tumor rapidly increased to approximately 62 °C within 5 min, which is sufficient destroy the cancer cells. In contrast, the tumor temperature of the NP_{DPT}, NP_{TVT}, and NP_{PhT} group only increased to 52 °C, 46 °C, and 40 °C, respectively.

The effect of these SPs with different A2 electron acceptor on *in vivo* PAI performance was detected with subcutaneous injections of matrigel-containing solutions of SP@NPs into the dorsal area of the same mouse. The PAI were acquired on the MSOT equipment (Figure 6C), and the quantitative PA intensities of these SP@NPs were illustrated in Figure 6D. There is no surprising that the NP_{TT} exhibits the highest PA signal among these SP@NPs, followed by NP_{DPT}, NP_{TVT}, and NP_{PhT}. and, the PA signal of NP_{TT} is ca. 5.8, 3.7, and 1.9 times brighter than that of NP_{DPT}, NP_{TVT}, and NP_{PhT}, respectively.

In vivo PAI and PTT performance of these SP@NPs

Encouraged by the excellent PT conversion and PA properties *in vivo*, PAI and PTT performances of SP@NPs were further studied. The SP@NPs were intravenously injected into mice bearing the MDA-MB-231 tumors through the tail vein at SP dose 40 μg per mice, and then the PA intensity in tumor tissue were recorded overtime by pulsed laser excitation at 808 nm. As shown in Figure 7A, the PA intensity of these SP@NPs gradually accumulated into tumor tissue, and reach its maximum at 2 h postinjection for all these SP@NPs. Then, the PA intensities progressively weaken. At all the time points, the NP_{TT} exhibited the highest PA intensity in the tumor area, followed by NP_{DPT}, NP_{TVT}, and NP_{PhT}. At 3 h postinjection (Figure 7B), and the PA intensity of NP_{TT} group was 1.30, 1.83, and 2.27 times brighter than that of NP_{DPT}, NP_{TVT}, and NP_{PhT}, respectively.

Following examination of the PAI of these SP@NPs *in vivo*, we further investigated their PT therapy abilities. The mice bearing the MDA-MB-231 tumor were injected with these nanoparticles containing 40 μg of SPs. Then, after 2 h postinjection, the NIR laser was used to irradiate the tumor site for 10 min, and then the tumor growth was monitored. As shown in Figure 8A, tumors injected with NP_{TT} plus NIR irradiation were significantly inhibited, and tumor growth was moderately inhibited for NP_{DPT} group. In contrast, the inhibition of tumor growth for the mice treated with NP_{TVT} or NP_{PhT} plus NIR irradiation was not noticeable. The above results were further confirmed by the representative mice photographs recorded before and after different treatments. Figure 8B demonstrated that excellent therapeutic effectiveness of the NP_{TT} groups could be clearly observed, leaving black scars at the original tumor sites (on the diseased tissue) at 14 days post-treatment. Moreover, it is worth noting that the injection of these formulations did not induce the change of body weight during the treatment (data not shown), indicating that the antitumor efficacy of these SP@NPs was not due to the cytotoxicity. Furthermore, the tumor mass was excised and imaged (Figure 8C) at the 14 days after the last measurement, and the weight of the tumor mass was assessed (Figure 8D). As expected, after treatment with NP_{TT} plus NIR irradiation, the weight of the tumor mass was the lowest, followed by NP_{DPT}, NP_{TVT} and NP_{PhT}, which showed the same order of the PT effect and PAI.

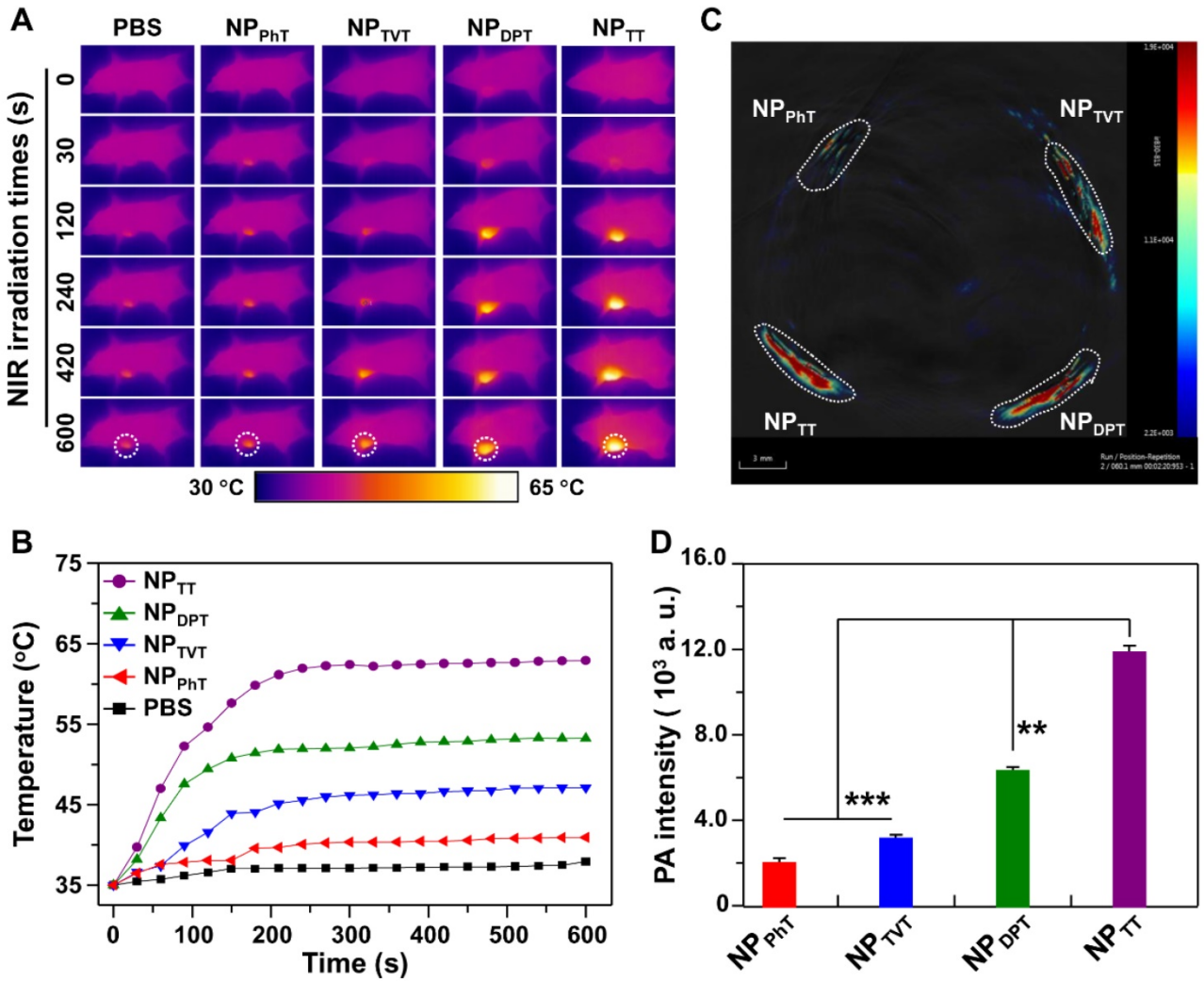

Figure 6. The PT effect and PAI properties of these SP@NPs *in vivo*. (A, B) Thermal images (A) and the temperature evolution on tumors (B) of MDA-MB-231 tumor-bearing mice after injection of SP@NPs (40 μg SP per mice) with NIR irradiation (808 nm, 0.5 W/cm², 10 min). (C, D) PA images (C) and amplitudes (D) of SP@NPs–matrigel inclusion (50 μg/mL, 30 μL) in the subcutaneous dorsal space of living mice. The images represent transverse slices through the subcutaneous inclusions. Error bars represent standard deviations of three separate measurements (n = 3).

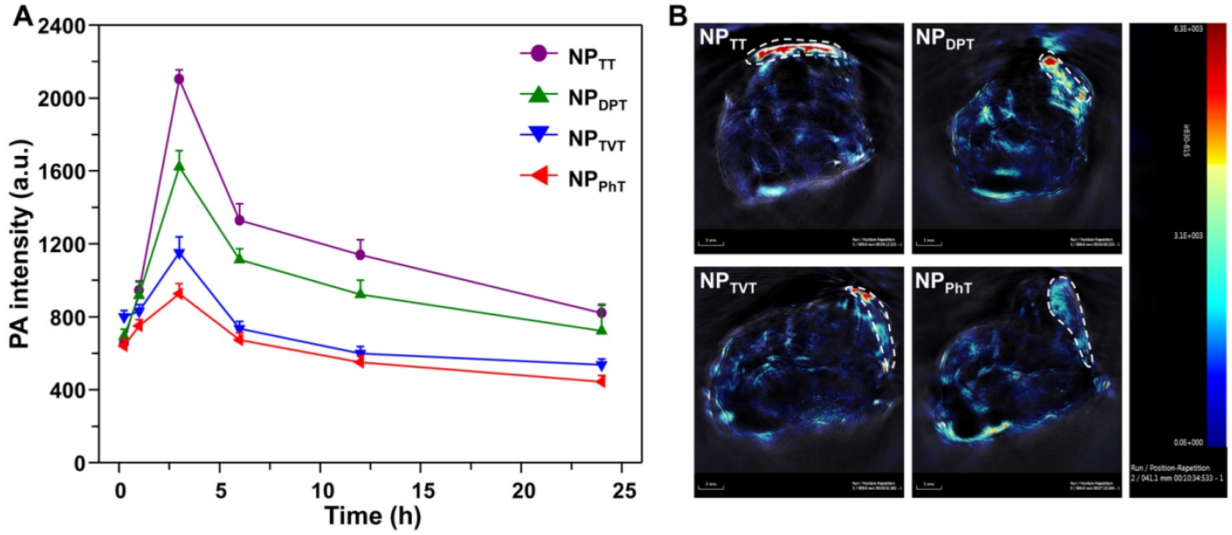

Figure 7. *In vivo* PA imaging of tumor with systemic administration of these SP@NPs. (A) PA signals at 808 nm in tumor as a function of time post-injection of these SP@NPs. All data are presented as mean ± SD (n = 3). (B) Representative PA maximum intensity projection of orthotopic breast cancer tumor model of a living mouse after intravenous injection of these SP@NPs. PA images were acquired at 808 nm, and tumor region was outlined in the white circle.

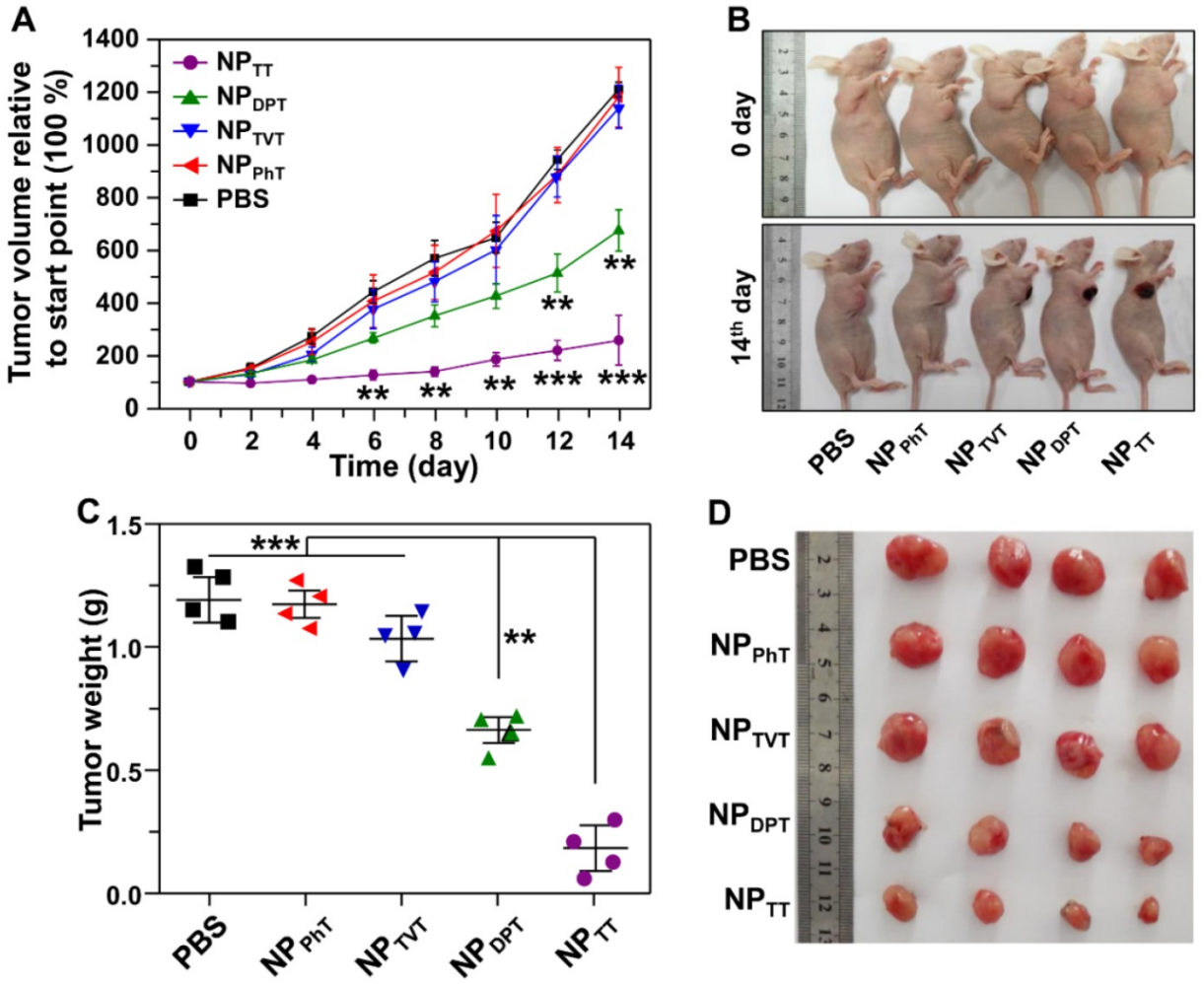

Figure 8. The PT therapy of these SP@NPs. (A) The MDA-MB-231 tumor growth curves of different groups of mice after intratumoral injection of SP@NPs (40 μg SP per mice) with NIR irradiation (808 nm, 0.5 W/cm^2, 10 min). (B) Representative pictures of mice before and on day 14 after PT therapy. (C) The weight of the tumors was assessed after the last determination (n = 4). (D) Photos of the tumors extracted from the mice bearing MDA-MB-231 tumor at the end of the experiment.

Conclusion

Herein, a series of acceptor–π–acceptor type SPs with variable chemical structure of A2 unit was used for PTT and PAI. These A1–π–A2 SPs were formulated into PEGylated nanoparticles through single emulsion methods with the assist of an amphiphilic copolymer, which ensured these SPs based nanoparticles exhibited similar size, shape, and physiological stability. Thus, the chemical structure of A2 unit was the only variable factor to be studied. We systematically and comprehensively demonstrated that the chemical structure of A2 unit significantly impact their absorption spectra and PT conversion efficiency, which finally determined their PT effect and PA brightness. It should be noted that the chemical structure of A1 unit and π-bridge could also impact their PTT and PAI performance. This study not only provides molecular insights into the design of efficient SPs for PTT and PAI but also highlights the flexibility and potential of SP@NPs for biomedical application. Thus, SP@NPs can act as a versatile nanoplatform for the development of novel light intensive imaging and therapeutic approaches.

Acknowledgements

This work was supported by the National Natural Science Foundation of China (51473043, 51773067, 51390482, and 51673190), the Natural Science Foundation for Distinguished Young Scholars of Guangdong Province, and the Fundamental Research Funds for the Central Universities. Dongdong Li, Guobing Zhang, and Weiguo Xu contributed equally to this work. The authors also acknowledge Prof. Jun Wang (South China University of Technology) and Xuesi Chen (Changchun Institute of Applied Chemistry, Chinese Academy of Sciences) for support.

Supplementary Material

Supplementary figures.
http://www.thno.org/v07p4029s1.pdf

Competing Interests

The authors have declared that no competing interest exists.

References

1. Kim JW, Galanzha EI, Shashkov EV, Moon HM, Zharov VP. Golden carbon nanotubes as multimodal photoacoustic and photothermal high-contrast molecular agents. Nat. Nanotechnol. 2009; 4: 688-94.
2. Lovell JF, Jin CS, Huynh E, Jin H, Kim C, Rubinstein JL, et al. Porphysome nanovesicles generated by porphyrin bilayers for use as multimodal biophotonic contrast agents. Nat. Mater. 2011; 10: 324-32.
3. Lyu Y, Fang Y, Miao Q, Zhen X, Ding D, Pu K. Intraparticle molecular orbital engineering of semiconducting polymer nanoparticles as amplified theranostics for in vivo photoacoustic imaging and photothermal therapy. ACS Nano 2016; 10: 4472-81.
4. Lyu Y, Xie C, Chechetka SA, Miyako E, Pu K. Semiconducting polymer nanobioconjugates for targeted photothermal activation of neurons. J. Am. Chem. Soc. 2016; 138: 9049-52.
5. Meng D, Yang S, Guo L, Li G, Ge J, Huang Y, et al. The enhanced photothermal effect of graphene/conjugated polymer composites: photoinduced energy transfer and applications in photocontrolled switches. Chem. Commun. 2014; 50: 14345-8.
6. Xiao L, Sun J, Liu L, Hu R, Lu H, Cheng C, et al. Enhanced photothermal bactericidal activity of the reduced graphene oxide modified by cationic water-soluble conjugated polymer. ACS Appl. Mater. Interfaces 2017; 9: 5382–91.
7. Chen M, Tang S, Guo Z, Wang X, Mo S, Huang X, et al. Core-shell Pd@Au nanoplates as theranostic agents for in-vivo photoacoustic imaging, ct imaging, and photothermal therapy. Adv. Mater. 2014; 26: 8210-6.
8. Huang P, Lin J, Li W, Rong P, Wang Z, Wang S, et al. Biodegradable gold nanovesicles with an ultrastrong plasmonic coupling effect for photoacoustic imaging and photothermal therapy. Angew. Chem. Int. Edn. 2013; 52: 13958-64.
9. Song J, Yang X, Jacobson O, Lin L, Huang P, Niu G, et al. Sequential drug release and enhanced photothermal and photoacoustic effect of hybrid reduced graphene oxide-loaded ultrasmall gold nanorod vesicles for cancer therapy. ACS Nano. 2015; 9: 9199-209.
10 Chen D, Wang C, Nie X, Li S, Li R, Guan M, et al. Photoacoustic imaging guided near-infrared photothermal therapy using highly water-dispersible single-walled carbon nanohorns as theranostic agents. Adv. Funct. Mater. 2014; 24: 6621-8.
11. Lee C, Kwon W, Beack S, Lee D, Park Y, Kim H, et al. Biodegradable nitrogen-doped carbon nanodots for non-invasive photoacoustic imaging and photothermal therapy. Theranostics. 2016; 6: 2196-208.
12. Ge J, Jia Q, Liu W, Guo L, Liu Q, Lan M, et al. Red-emissive carbon dots for fluorescent, photoacoustic, and thermal theranostics in living mice. Advanced Materials. 2015; 27: 4169-77.
13. Zhang L, Gao S, Zhang F, Yang K, Ma Q, Zhu L. Activatable hyaluronic acid nanoparticle as a theranostic agent for optical/photoacoustic image-guided photothermal therapy. ACS Nano. 2014; 8: 12250-8.
14. Liu R, Jing L, Peng D, Li Y, Tian J, Dai Z. Manganese (II) chelate functionalized copper sulfide nanoparticles for efficient magnetic resonance/photoacoustic dual-modal imaging guided photothermal therapy. Theranostics. 2015; 5: 1144-53.
15. Ku G, Zhou M, Song S, Huang Q, Hazle J, Li C. Copper sulfide nanoparticles as a new class of photoacoustic contrast agent for deep tissue imaging at 1064 nm. ACS Nano. 2012; 6: 7489-96.
16. Liang XL, Li YY, Li XD, Jing LJ, Deng ZJ, Yue XL, et al. Pegylated polypyrrole nanoparticles conjugating gadolinium chelates for dual-modal mri/photoacoustic imaging guided photothermal therapy of cancer. Adv. Funct. Mater. 2015; 25: 1451-62.
17. Su S, Ding Y, Li Y, Wu Y, Nie G. Integration of photothermal therapy and synergistic chemotherapy by a porphyrin self-assembled micelle confers chemosensitivity in triple-negative breast cancer. Biomaterials. 2016; 80: 169-78.
18. Muhanna N, Jin CS, Huynh E, Chan H, Qiu Y, Jiang W, et al. Phototheranostic porphyrin nanoparticles enable visualization and targeted treatment of head and neck cancer in clinically relevant models. Theranostics. 2015; 5: 1428-43.
19. Chen Q, Liu X, Zeng J, Cheng Z, Liu Z. Albumin-NIR dye self-assembled nanoparticles for photoacoustic pH imaging and pH-responsive photothermal therapy effective for large tumors. Biomaterials. 2016; 98: 23-30.
20. Caixia Y, Peng L, Mingbin Z, Pengfei Z, Yiqing W, Yifan M, et al. IR-780 dye loaded tumor targeting theranostic nanoparticles for NIR imaging and photothermal therapy. Biomaterials. 2013; 34: 6853-61.
21. Sheng Z, Hu D, Zheng M, Zhao P, Liu H, Gao D, et al. Smart human serum albumin-indocyanine green nanoparticles generated by programmed assembly for dual-modal imaging-guided cancer synergistic phototherapy. ACS Nano. 2014; 8: 12310-22.
22. Pu K, Mei J, Jokerst JV, Hong G, Antaris AL, Chattopadhyay N, et al. Diketopyrrolopyrrole-based semiconducting polymer nanoparticles for in vivo photoacoustic imaging. Adv. Mater. 2015; 27: 5184-90.
23. Li S, Wang X, Hu R, Chen H, Li M, Wang J, et al. Near-infrared (NIR)-absorbing conjugated polymer dots as highly effective photothermal materials for *in vivo* cancer therapy. Chem. Mater. 2016; 28: 8669-75.
24. Li DD, Wang JX, Ma Y, Qian SH, Wang D, et al. A donor−acceptor conjugated polymer with alternating isoindigo derivative and bithiophene units for near-infrared modulated cancer thermo-chemotherapy. ACS Appl. Mater. Interfaces 2016; 8: 19312-20.
25. Ng KK, Lovell JF, Vedadi A, Hajian T, Zheng G. Self-assembled porphyrin nanodiscs with structure-dependent activation for phototherapy and photodiagnostic applications. ACS Nano. 2013; 7: 3484-90.
26. Guenes S, Neugebauer H, Sariciftci NS. Conjugated polymer-based organic solar cells. Chem. Rev.. 2007; 107: 1324-38.
27. Heeger AJ. Semiconducting polymers: the third generation. Chem. Soc. Rev. 2010; 39: 2354-71.
28. Liang Y, Yu L. A new class of semiconducting polymers for bulk heterojunction solar cells with exceptionally high performance. Acc. Chem. Res. 2010; 43: 1227-36.
29. Lin Y, Li Y, Zhan X. Small molecule semiconductors for high-efficiency organic photovoltaics. Chem. Soc. Rev. 2012; 41: 4245-72.
30. Pu K, Shuhendler AJ, Jokerst JV, Mei J, Gambhir SS, Bao Z, et al. Semiconducting polymer nanoparticles as photoacoustic molecular imaging probes in living mice. Nat. Nanotechnol. 2014; 9: 233-9.
31. Lyu Y, Zhen X, Miao Y, Zhen X, Ding D, Pu K. Reaction-based semiconducting polymer nanoprobes for photoacoustic imaging of protein sulfenic acids. ACS Nano. 2017; 11: 358-67.
32. Jing Z, Zhigao L, Xingjun Z, Xuejiao W, Yi L, Zhanfang M, et al. NIR photothermal therapy using polyaniline nanoparticles. Biomaterials. 2013; 34: 9584-92.
33. Wang J, Tan X, Pang X, Liu L, Tan F, Li N. MoS2 quantum dot@polyaniline inorganic-organic nanohybrids for in vivo dual-modal imaging guided synergistic photothermal/radiation therapy. ACS Appl. Mater. Interfaces 2016; 8: 24331-8.
34. Hua G, Liang C, Jian X, Huan X, Liangzhu F, Xiaoze S, et al. Near-infrared absorbing polymeric nanoparticles as a versatile drug carrier for cancer combination therapy. Adv. Func. Mater. 2013; 23: 6059-67.
35. Cheng L, Yang K, Chen Q, Liu Z. Organic stealth nanoparticles for highly effective in vivo near-infrared photothermal therapy of cancer. ACS Nano. 2012; 6: 5605-13.
36. Song XJ, Gong H, Yin SN, Cheng L, Wang C, Li ZW, et al. Ultra-small iron oxide doped polypyrrole nanoparticles for in vivo multimodal imaging guided photothermal therapy. Adv. Func. Mater. 2014; 24: 1194-201.
37. Zha Z, Yue X, Ren Q, Dai Z. Uniform polypyrrole nanoparticles with high photothermal conversion efficiency for photothermal ablation of cancer cells. Adv. Mater. 2013; 25: 777-82.
38. Wang C, Xu H, Liang C, Liu Y, Li Z, Yang G, et al. Iron oxide @ polypyrrole nanoparticles as a multifunctional drug carrier for remotely controlled cancer therapy with synergistic antitumor effect. ACS Nano. 2013; 7: 6782-95.
39. Miao Q, Lyu Y, Ding D, Pu K. Semiconducting oligomer nanoparticles as an activatable photoacoustic probe with amplified brightness for in vivo imaging of pH. Adv. Mater. 2016; 28: 3662-8.
40. Pu K, Chattopadhyay N, Rao J. Recent advances of semiconducting polymer nanoparticles in in vivo molecular imaging. J. Controlled Release. 2016; 240: 312-22.
41. Braslavsky SE, Heibel GE. Time-resolved photothermal and photoacoustic methods applied to photoinduced processes in solution. Chem. Rev. 1992; 92: 1381−410.
42. Roper DK, Ahn W, Hoepfner M. Microscale heat transfer transduced by surface plasmon resonant gold nanoparticles. J. Phys. Chem. C. 2007; 111: 3636-41.
43. Zhang G, Guo J, Zhang J, Li P, Ma J, Wang X, et al. A phthalimide- and diketopyrrolopyrrole-based A(1)-pi-A(2) conjugated polymer for high-performance organic thin-film transistors. Polym. Chem. 2015; 6: 418-25.